photonics

MDPI

Article

Planar-Symmetric Fore-Afocal Lens Mapping for Residual Motion Compensation Error Suppression in Backscanning Step-and-Stare Imaging

Yang Liu [1,*], Yuanlin Cui [2], Lujia Wang [1], Xiang Chen [1], Zhenyan Hou [1], Xiangyun Liu [1] and Jing Jia [1]

[1] Southwest Institute of Technical Physics, No. 7, Renmin South Road, Chengdu 610041, China
[2] College of Teacher Education, Sichuan University of Arts and Science, No. 519, Tashi Road, Dazhou 635000, China
* Correspondence: liuyang1.2005@tsinghua.org.cn

Abstract

Fore-afocal lenses with axisymmetric and linear angular magnifications are widely used for ray-beam compression before retrace compensation in backscanning step-and-stare imaging. However, the axisymmetric nature of the fore-afocal lens mapping introduces differences in the motion characteristics of off-axis rays relative to the central field, thereby leading to residual motion compensation errors and motion blur at off-axis positions within the instantaneous field of view (IFOV). To overcome this limitation, we derive a planar-symmetric fore-afocal lens mapping that ensures uniform rotational behavior of the output rays during scanning. Combined with image-space retrace compensation, this mapping theoretically enables residual motion compensation error suppression across the full IFOV. We further present an optical design implementation method for this mapping using a freeform field lens group and validate the theory and method through comprehensive optical simulations and comparative analyses, using a mid-wave infrared backscanning step-and-stare imaging system as a case study. Under operating conditions of a 400°/s scanning speed and a 5 ms exposure time in a simulation environment, the maximum motion blur caused by the residual motion compensation error is reduced from 607 μm to 3.1 μm compared with the axisymmetric case, confirming the effectiveness of the theory and methodology. The proposed planar-symmetric fore-afocal lens mapping is broadly applicable to backscanning step-and-stare imaging systems with a wide IFOV, substantially enhancing their off-axis imaging performance.

Keywords: step-and-stare imaging; motion blur; planar-symmetric; freeform lens

Check for updates

Received: 25 September 2026
Revised: 23 October 2026
Accepted: 28 October 2026
Published: 30 October 2026

Copyright: © 2026 by the authors. Licensee MDPI, Basel, Switzerland. This article is an open access article distributed under the terms and conditions of the Creative Commons Attribution (CC BY) license.

1. Introduction

Backscanning step-and-stare imaging systems equipped with staring-array detectors are widely used owing to their wide IFOVs and high scanning efficiency [1–3]. Such systems adopt a typical configuration consisting of a fore-afocal lens, a retrace mirror (typically a galvanometer or a fast steering mirror), an imaging lens, and a staring-array detector [4–8], as shown in Figure 1. The fore-afocal lens compresses the incident collimated ray beams and outputs smaller-aperture collimated ray beams with their angles magnified. The retrace mirror is placed at the exit pupil of the afocal lens to avoid pupil shift during retracing, while also minimizing its size and weight to ensure dynamic compensation performance [5]. As the system scans continuously with an angular rate of w, the mirror retraces at $mw/2$ during the exposure time (m is the angular magnification of the fore-afocal lens) to maintain the

line of sight (LOS), thereby enabling stare imaging over the current IFOV [6]. After the current exposure, the retrace mirror rapidly returns to its initial position, and the process repeats for the next IFOV. Since the retrace mirror is located on the image side, it is referred to as image-space retrace compensation (as opposed to object-space retrace compensation, where the mirror is placed at the entrance pupil in front of the lens). The basic configuration and operating principle are illustrated in Figure 1.

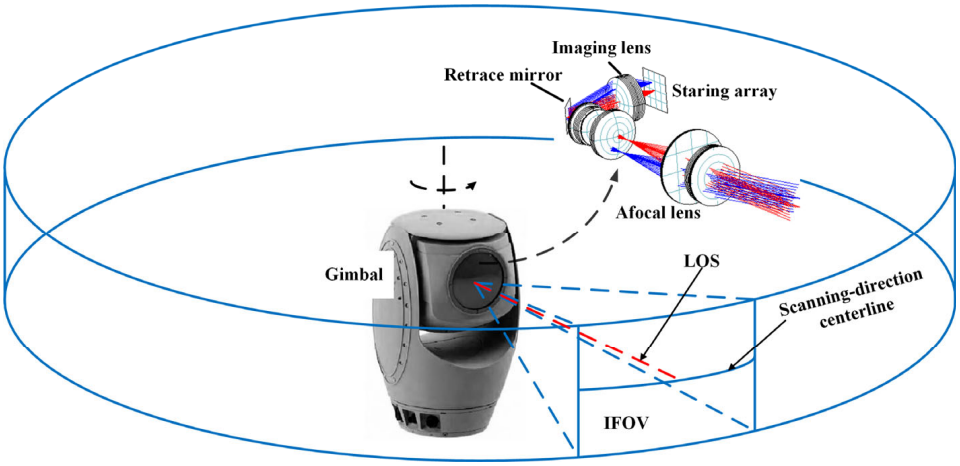


Figure 1. The basic configuration and operating principle of backscanning step-and-stare imaging with image-space retrace compensation.

During operation, the fore-afocal lens forms an image at infinity of an object, with both the input and output ray beams collimated. There is a one-to-one direction mapping relationship between the output rays and the input rays. This relationship is referred to as the fore-afocal lens mapping in this paper. In practice, the fore-afocal lens generally adopts an axisymmetric Keplerian design, with good linear angular magnification to ensure linearity during retrace compensation [5], and the mapping exhibits axisymmetric characteristics.

As shown in Figure 2, let the Y-axis be the scanning axis and the XZ-plane the scanning plane. Platform rotation can be equivalent to an object point moving along a circular arc curve parallel to the XZ-plane on a cylindrical surface A at infinity centered on the Y-axis. And retrace compensation can be equivalent to the image point moving oppositely on a magnified cylindrical surface B at infinity centered on the Y-axis, also along a circular arc curve parallel to the XZ-plane. Figure 2 illustrates the motion characteristics of the central field chief ray and an off-axis field chief ray during scanning. For complete motion compensation, the intersection of the output chief ray with surface B must coincide dynamically and exactly with the retrace compensation equivalent motion curve. This essentially requires the fore-afocal lens to image cylindrical surface A onto cylindrical surface B, which demands different horizontal and vertical magnifications and thus contradicts the axisymmetric mapping property. Only object points in the central field and those on the scanning-direction centerline satisfy the complete compensation condition, since their output chief rays are angularly magnified in the XZ plane and strictly rotate at mw about the Y-axis. For an off-axis field position outside the scanning-direction centerline, the angular magnification direction lies in an oblique meridional plane. As its inclination angle u varies with time during scanning, the magnifications projected onto the horizontal and vertical directions become time-varying quantities. Consequently, the intersection of the output chief ray with surface B does not rotate strictly about the scanning axis at mw during scanning. It exhibits dynamic deviations in both the scan and cross-scan directions relative to the retrace compensation equivalent motion curve, as shown by the magnified view in the upper-left corner of Figure 2. Therefore, under axisymmetric fore-afocal lens mapping, complete

motion compensation cannot be achieved for these off-axis field positions, and residual compensation errors inevitably remain.

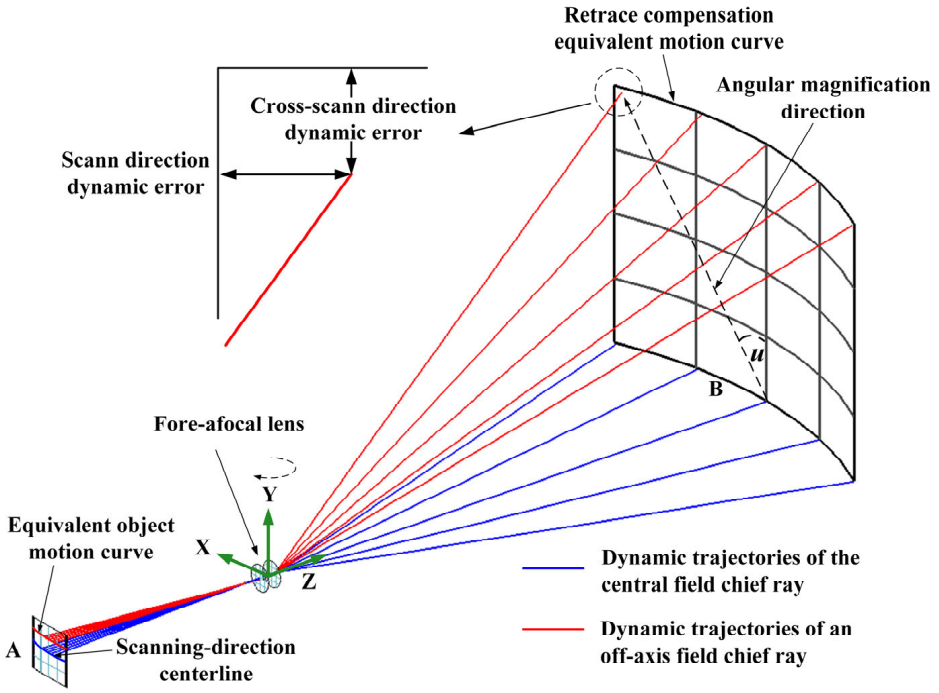


Figure 2. Schematic illustration of the motion characteristics of the input and output chief rays of the axisymmetric fore-afocal lens during scanning.

Considerable research has been devoted to motion compensation for backscanning step-and-stare imaging, including optimization of retrace compensation control algorithms and multichannel bilateral compensation control [9–11]. However, these approaches do not account for the disparity in motion behavior between the off-axis fields and the central field. Yunxi Li et al. proposed a dual-galvanometer compensation method that can correct scanning error at different field angles [12]. Nevertheless, this method is restricted to point-by-point correction and is not applicable to systems using staring arrays. Edward A. Dehoog adopted a rotating-cylindrical-lens approach for dynamic compensation [13], yet this technique is limited to single-beam operation and cannot simultaneously correct multiple field positions.

To the best of our knowledge, no existing method can effectively solve the residual motion compensation error problem discussed above. To resolve this issue, this paper derives and proposes a planar-symmetric fore-afocal lens mapping, which guarantees that the output rays exhibit identical rotational motion about the scanning axis for all field positions within the IFOV throughout gimbal rotation. When combined with image-space retrace, it theoretically enables residual motion compensation error suppression across the full IFOV. We further discuss the optical design implementation of this mapping. Freeform optical elements offer high design flexibility and strong field-controlling capabilities, and considerable research has been devoted successfully to the design of asymmetric object-image mappings using freeform optics [14,15]. Accordingly, we employ freeform optics for the optical design implementation. Following the approach of H.J. Mann et al. [16], we introduce a freeform field lens group into the original axisymmetric afocal lens and realize the desired planar-symmetric mapping via optical optimization.

The effectiveness of the proposed theory and method is validated through comprehensive optical simulations and comparative analyses, conducted with a mid-wave infrared backscanning step-and-stare imaging system as a case study. Static and scanning simulations are carried out using both the axisymmetric and planar-symmetric designs. The results show that when the planar-symmetric fore-afocal lens mapping is employed, the maximum residual motion blur across the IFOV is reduced from 607 μm to 3.1 μm compared to the axisymmetric case in a simulation environment, revealing that the residual motion compensation error across the full IFOV is effectively mitigated and confirming the effectiveness of the theory and method proposed in this work.

2. Theoretical Derivations

2.1. Residual Motion Compensation Error Under Axisymmetric Fore-Afocal Lens Mapping

As discussed in Section 1 with Figure 2, the residual motion compensation error arises because the axisymmetric fore-afocal lens mapping (the directional mapping relationship between input and output ray beams) prevents off-axis field output rays from rotating uniformly about the rotation axis at the magnified angular rate. Such motion cannot be fully compensated by retrace compensation, leaving inevitable residual errors at off-axis fields. This subsection provides a rigorous theoretical derivation and quantitative analysis, with directional tangents used to represent the ray directions.

Figure 3 presents the schematic of backscanning step-and-stare imaging with the scanning plane defined as the X–Z plane and the rotation axis as the *Y*-axis. Taking the midpoint of the exposure time T as the reference and letting t denote the temporal time during a single-frame exposure, the instantaneous rotation angle θ of the gimbal is given by:

$$\theta = wt \tag{1}$$

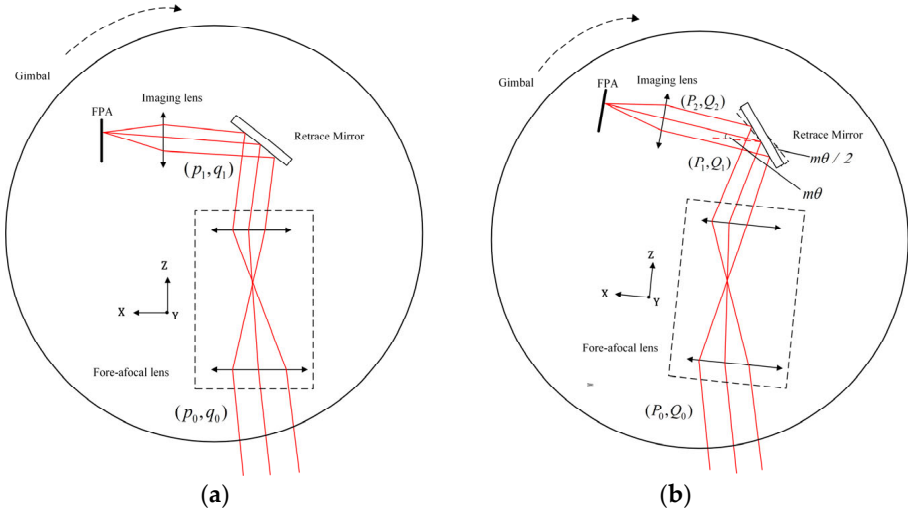


Figure 3. Schematic of the backscanning step-and-stare imaging. (**a**) The gimbal and retrace mirror are static and at zero positions. (**b**) The gimbal scans by an instantaneous angle θ, and the mirror retraces by $m\theta/2$.

As illustrated in Figure 3a, when the system is static with the gimbal at zero position ($\theta = 0$), consider an input ray beam with directional tangents (p_0,q_0) from an arbitrary object field point. The ray beam is collected by the fore-afocal lens and then output with angular magnification, with directional tangents denoted as (p_1,q_1). Under axisymmetric fore-afocal lens mapping, the incident chief ray, the outgoing chief ray, and the optical axis

are coplanar, and the angle subtended by the outgoing chief ray with the optical axis equals m times that of the incident chief ray. Therefore, (p_1,q_1) and (p_0,q_0) are related as follows:

$$\begin{aligned} &\cos^{-1}\left(\left({p_1}^2+{q_1}^2+1\right)^{-1/2}\right) = m\cos^{-1}\left(\left({p_0}^2+{q_0}^2+1\right)^{-1/2}\right) \\ &(p_0,q_0,1)\times(0,0,1)\cdot(p_1,q_1,1)=0 \end{aligned} \tag{2}$$

From the above expressions, the mapping relationship from (p_0,q_0) to (p_1,q_1) is derived as:

$$\begin{aligned} p_1 &= p_0\left({p_0}^2+{q_0}^2\right)^{-1/2}\tan\left(m\ \cos^{-1}\left(\left({p_0}^2+{q_0}^2+1\right)^{-1/2}\right)\right) \\ q_1 &= q_0\left({p_0}^2+{q_0}^2\right)^{-1/2}\tan\left(m\ \cos^{-1}\left(\left({p_0}^2+{q_0}^2+1\right)^{-1/2}\right)\right) \end{aligned} \tag{3}$$

As illustrated in Figure 3b, consider the gimbal is rotated by an instantaneous angle $\theta = wt$. The input ray-beam directional tangents from the same object field point, expressed in the local coordinate system of the fore-afocal lens, change to (P_0,Q_0) and can be obtained by rotating the ray beam corresponding to (p_0,q_0) by $-wt$ about the Y-axis:

$$P_0 = \frac{p_0\cos wt+\sin wt}{-p_0\sin wt+\cos wt},\ Q_0 = \frac{q_0}{-p_0\sin wt+\cos wt} \tag{4}$$

Let the directional tangents of the corresponding output ray beam be denoted by (P_1,Q_1). They are obtained by substituting P_0 for p_0 and Q_0 for q_0 in Equation (3) and rearranged as:

$$\begin{aligned} P_1 &= \frac{p_0\cos wt+\sin wt}{\sqrt{{q_0}^2+{p_0}^2\ \cos^2\ wt+p_0\sin(2wt)+\sin^2 wt}}\tan\left(m\ \cos^{-1}\frac{\cos wt-p_0\sin wt}{\sqrt{{p_0}^2+{q_0}^2+1}}\right) \\ Q_1 &= \frac{q_0}{\sqrt{{q_0}^2+{p_0}^2\ \cos^2\ wt+p_0\sin(2wt)+\sin^2 wt}}\tan\left(m\ \cos^{-1}\frac{\cos wt-p_0\sin wt}{\sqrt{{p_0}^2+{q_0}^2+1}}\right) \end{aligned} \tag{5}$$

Equation (5) describes the temporal behavior of the output ray beam under axisymmetric fore-afocal lens mapping. As shown in Figure 3b, compensation is performed by counter-rotating the retrace mirror. At the instantaneous time t, the retrace compensation is equivalent to rotating the ray beam corresponding to (P_1,Q_1) by $-mwt$ about the Y-axis; the directional tangents of the ray beam after retrace compensation, denoted as (P_2,Q_2), are related to (P_1,Q_1) through a spatial vector rotation as follows:

$$P_2 = \frac{P_1\cos(mwt)+\sin(mwt)}{-P_1\sin(mwt)+\cos(mwt)},\ Q_2 = \frac{Q_1}{-P_1\sin(mwt)+\cos(mwt)} \tag{6}$$

Equation (6) can be rewritten and rearranged as:

$$(P_2,Q_2) = (P_1,Q_1)-(P_c,Q_c) = (p_1,q_1)+(\delta P,\delta Q) \tag{7}$$

where $(P_c,Q_c) = (P_1-P_2,Q_1-Q_2)$ represents the compensation amount introduced by the retrace mirror, and $(\delta P,\delta Q) = (P_2-p_1,Q_2-q_1)$ represents the residual motion compensation error of the ray beam after compensation. From Equations (3)–(6), the analytical expressions for δP and δQ can be derived; since the expressions are lengthy and complex, they are not directly given here. As the instantaneous platform rotation angle wt within a single-frame exposure is small, series expansions of δP and δQ are performed with only the first- and second-order terms in wt retained, yielding the approximate and simplified expressions for δP and δQ as follows:

$$\begin{aligned} \delta P &\approx \left(-\frac{m{q_0}^2}{{p_0}^2+{q_0}^2}+\frac{{q_0}^2}{\left({p_0}^2+{q_0}^2\right)^{3/2}}\tan\left(m\ \cos^{-1}\frac{1}{\sqrt{{p_0}^2+{q_0}^2+1}}\right)\right)wt \\ \delta Q &\approx \left(\frac{mp_0q_0}{{p_0}^2+{q_0}^2}-\frac{p_0q_0}{\left({p_0}^2+{q_0}^2\right)^{3/2}}\tan\left(m\ \cos^{-1}\frac{1}{\sqrt{{p_0}^2+{q_0}^2+1}}\right)\right)wt-\frac{m^3-m}{6}q_0(wt)^2 \end{aligned} \tag{8}$$

The ray beam after compensation is focused by the imaging lens onto the detector plane. This process converts the residual motion compensation error (angular error) into motion blur (linear error) on the focal plane. Let f denote the focal length of the entire scanning imaging system; the focal length of the imaging lens group is then f/m. Let δl_x and δl_y denote the horizontal and vertical dynamic motion blur on the focal plane; the calculation formula is given by:

$$\left(\delta l_x, \delta l_y\right) = \left(\frac{f}{m}\delta P, \frac{f}{m}\delta Q\right) \tag{9}$$

Although Equation (8) shows simplified formulas based on low-order approximations, a more rigorous theoretical analysis shows that for a platform rotation angle $|wt| \leq 5°$ during exposure (covering most backscanning step-and-stare imaging systems), the result from Equation (8) deviates from those of the original formula by no more than 2%, which is sufficient for analysis and evaluation. Moreover, the linear term in wt, the quadratic terms in combinations of p_0 and q_0, and the m^2 term dominate in Equations (8) and (9). Consequently, the motion blur caused by the residual compensation error grows approximately linearly with scanning speed and integration time, quadratically with field position and the fore-afocal lens magnification.

Using Equations (3)–(8), we compute the dynamic motion curves, compensation curves, and residual motion compensation errors of the output ray beams for multiple field positions under two different operating conditions. The first operating condition is: magnification $m = 8$, IFOV = 4° × 4°, scanning rate $w = 400°/s$, and exposure time $T = 5$ ms. The second operating condition is: magnification $m = 4$, IFOV = 15° × 15°, scanning rate $w = 400°/s$, and exposure time $T = 9$ ms. Figure 4a,c present the ray beam motion curves and retrace compensation curves under the two operating conditions, from which it can be seen that differences exist between the motion curves and retrace compensation curves for off-axis field positions not on the centerline. Figure 4b,d present the residual motion compensation errors under the two operating conditions, which reach maximum values of 10 mrad and 75 mrad, respectively, at the diagonal marginal field positions—levels that could cause significant image blur in practical use.

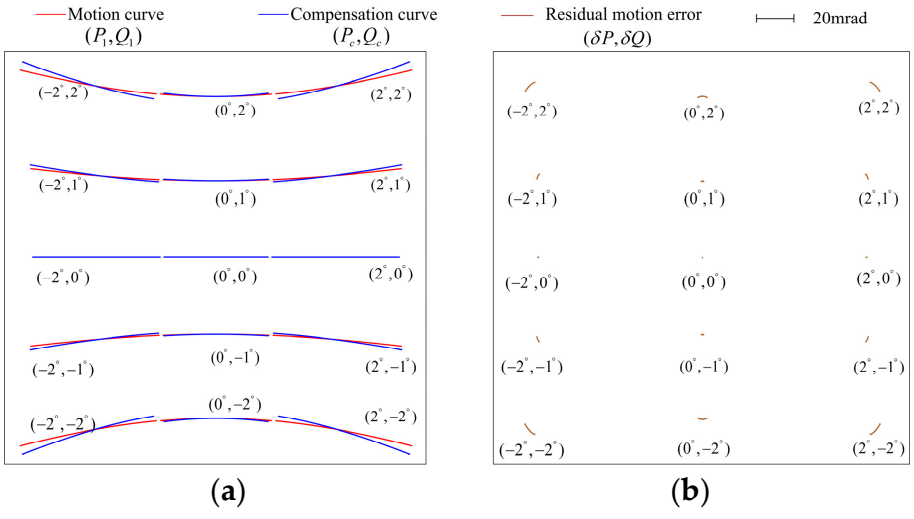


Figure 4. *Cont.*

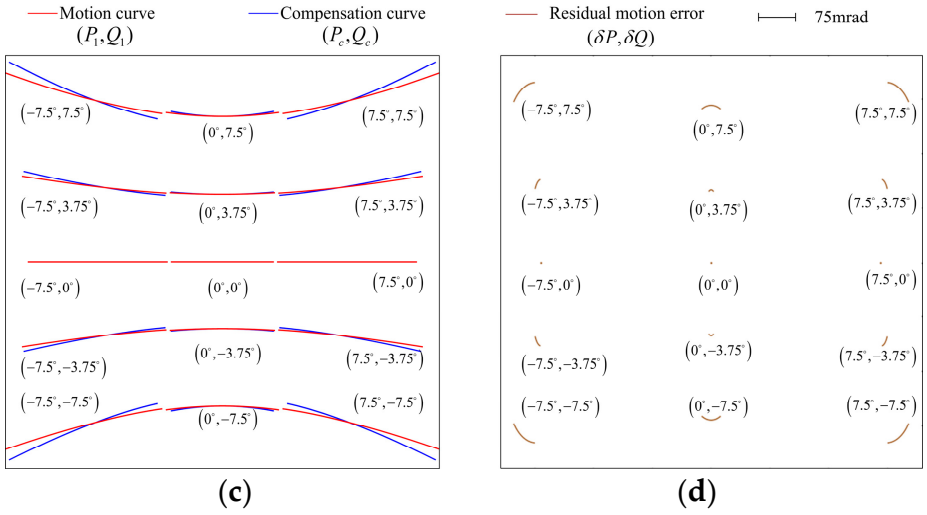


Figure 4. The dynamic motion curves, compensation curves, and residual motion compensation errors in backscanning step-and-stare imaging with an axisymmetric fore-afocal lens. (**a**) The dynamic motion curves and compensation curves, $m = 8$, IFOV = 4° × 4°, $w = 400°/s$, $T = 5$ ms. (**b**) The residual motion compensation errors, $m = 8$, IFOV = 4° × 4°, $w = 400°/s$, $T = 5$ ms. (**c**) The dynamic motion curves and compensation curves, $m = 4$, IFOV = 15° × 15°, $w = 720°/s$, $T = 9$ ms. (**d**) The residual motion compensation errors, $m = 4$, IFOV = 15° × 15°, $w = 720°/s$, $T = 9$ ms.

2.2. Planar-Symmetric Fore-Afocal Lens Mapping for Residual Motion Compensation Error Suppression

Section 2.1 provides a detailed theoretical derivation and analysis of the residual motion compensation error under conventional axisymmetric fore-afocal lens mapping. These errors cause motion blur on the image plane. Although it may be possible to reduce these errors by directly optimizing the optical design parameters, such an approach lacks general theoretical guidance. Based on the mechanism by which the error arises, this subsection derives and presents a planar-symmetric fore-afocal lens mapping that eliminates the residual motion compensation errors at its source.

The fundamental solution to the residual motion compensation error problem lies in seeking a new mapping for the fore-afocal lens that ensures the output rays from any object point within the IFOV undergo uniform rotation about the scanning axis at the magnified angular rate mw. Assuming the existence of such a mapping, with operators denoted as M_x and M_y. When the system is static, for the input ray beam with directional tangents (p_0,q_0) (see Figure 3a), the corresponding output ray-beam directional tangents under the new mapping, denoted as (p_1^*,q_1^*), are given by:

$$p_1^* = M_x(p_0,q_0),\ q_1^* = M_y(p_0,q_0) \tag{10}$$

When the gimbal is rotated by an instantaneous angle wt, the input ray-beam directional tangents expressed in the local coordinate system change to (P_0,Q_0) (see Figure 3b), and the output ray-beam directional tangents of the new mapping, change to (P_1^*,Q_1^*), are given by:

$$P_1^* = M_x(P_0,Q_0),\ Q_1^* = M_y(P_0,Q_0) \tag{11}$$

To ensure the output rays from different field positions rotate uniformly about the scanning axis at the magnified angular rate, the following condition must hold: at time t, the dynamical output ray beam of the mapping (with directional tangents (P_1^*,Q_1^*)) must

exactly coincide in direction with the static output ray beam (with directional tangents $(p_1{}^*,q_1{}^*)$) after the latter is rotated by $-mwt$ about the scanning rotation axis:

$$(P_1{}^*,Q_1{}^*) == \left(\frac{p_1{}^*\cos(mwt)+\sin(mwt)}{-p_1{}^*\sin(mwt)+\cos(mwt)}, \frac{q_1{}^*}{-p_1{}^*\sin(mwt)+\cos(mwt)}\right) \tag{12}$$

Using Equations (4), (10) and (11), Equation (12) can be rearranged and rewritten as the following conditions:

$$\begin{aligned} \mathcal{M}_x\left(\frac{p_0\cos wt+\sin wt}{-p_0\sin wt+\cos wt}, \frac{q_0}{-p_0\sin wt+\cos wt}\right) &== \frac{\mathcal{M}_x(p_0,q_0)\cos(mwt)+\sin(mwt)}{-\mathcal{M}_x(p_0,q_0)\sin(mwt)+\cos(mwt)} \\ \mathcal{M}_y\left(\frac{p_0\cos wt+\sin wt}{-p_0\sin wt+\cos wt}, \frac{q_0}{-p_0\sin wt+\cos wt}\right) &== \frac{\mathcal{M}_y(p_0,q_0)}{-\mathcal{M}_x(p_0,q_0)\sin(mwt)+\cos(mwt)} \end{aligned} \tag{13}$$

Equation (13) forms a complex mathematical-physical equation system that cannot be solved directly. According to the research findings by LIU et al. [17], as the "parabasal" property of rays, the object-image mapping of an optical system can be expressed as a product of series expansions, each depending on an independent variable. Therefore, the separation-of-variables method is applied to derive the analytical expressions for $\mathcal{M}_x(p_0,q_0)$ and $\mathcal{M}_y(p_0,q_0)$. The detailed derivations are given in Appendix A; here we directly give the results, as follows:

$$\mathcal{M}_x(p_0,q_0) == \tan\left(m\ \tan^{-1}p_0\right),\ \mathcal{M}_y(p_0,q_0) == m\frac{\cos\left(\tan^{-1}p_0\right)}{\cos\left(m\ \tan^{-1}p_0\right)}q_0 \tag{14}$$

For a 4° × 4° IFOV, Figure 5 presents the mapping grids obtained from Equation (14) for various magnifications m. The new mapping clearly shows different magnifications along the horizontal and vertical directions, exhibiting planar-symmetric anamorphic characteristics.

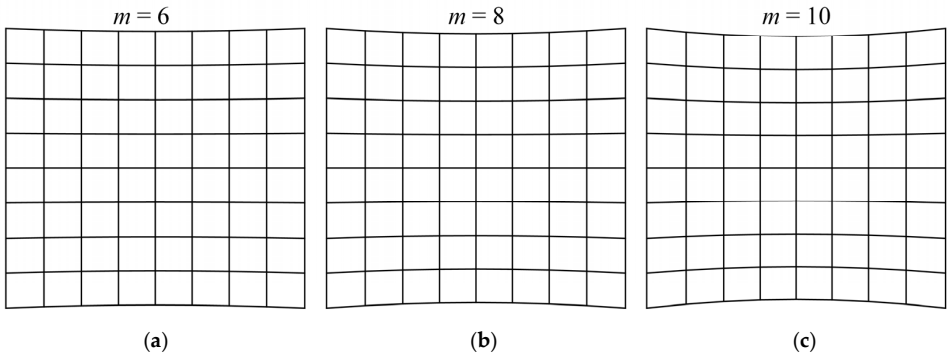


Figure 5. The planar-symmetric fore-afocal lens mapping grids for a 4° × 4° instantaneous field of view. (**a**) $m = 6$. (**b**) $m = 8$. (**c**) $m = 10$.

To intuitively describe the effectiveness of the new mapping in eliminating residual motion compensation errors, it is necessary to analyze the motion characteristics, the retrace compensation amount, and the residual motion of the output ray beams under the new mapping. The dynamic angular motion of the output ray beams is given by Equation (12). Let $(P_2{}^*,Q_2{}^*)$ denote the directional tangents of the ray beams after retrace compensation; they can be obtained by substituting $P_1{}^*$ for P_1 and $Q_1{}^*$ for Q_1 in Equation (6):

$$P_2{}^* = \frac{P_1{}^*\cos(mwt)+\sin(mwt)}{-P_1{}^*\sin(mwt)+\cos(mwt)},\ Q_2{}^* = \frac{Q_1{}^*}{-P_1{}^*\sin(mwt)+\cos(mwt)} \tag{15}$$

Similar to Equation (7), Equation (15) can be rewritten as:

$$(P_2{}^*,Q_2{}^*) = (P_1{}^*,Q_1{}^*) - (P_c{}^*,Q_c{}^*) = (p_1{}^*,q_1{}^*) + (\delta P^*,\delta Q^*) \tag{16}$$

where $(P_c{}^*,Q_c{}^*) = (P_1{}^* - P_2{}^*,Q_1{}^* - Q_2{}^*)$ denotes the retrace compensation amount applied to the output ray beam under the planar-symmetric fore-afocal lens mapping, and

$(\delta P^*,\delta Q^*) = (P_2^* - p_1^*, Q_2^* - q_1^*)$ represents the residual motion compensation error under the planar-symmetric fore-afocal lens mapping. From Equations (4), (10), (12), (14) and (15), it can be derived that δP^* and δQ^* are strictly equal to zero.

For comparison with the compensation performance under axisymmetric fore-afocal lens mapping, analysis is performed here under the two identical operating conditions described in Section 2.1. Equations (4), (10), (12) and (14)–(16) are used to compute the dynamic motion curves, compensation curves, and residual motion compensation errors of output ray beams under the planar-symmetric fore-afocal lens mapping. Figure 6a,c present the ray-beam motion curves and retrace compensation curves under the two operating conditions, from which it can be seen that the motion curves coincide with the corresponding compensation curves. Figure 6b,d present the residual motion compensation errors under the two operating conditions; clearly, all the ray beams remain stationary after retrace compensation, with their motion trajectories collapsing to points and residual motion compensation errors effectively mitigated.

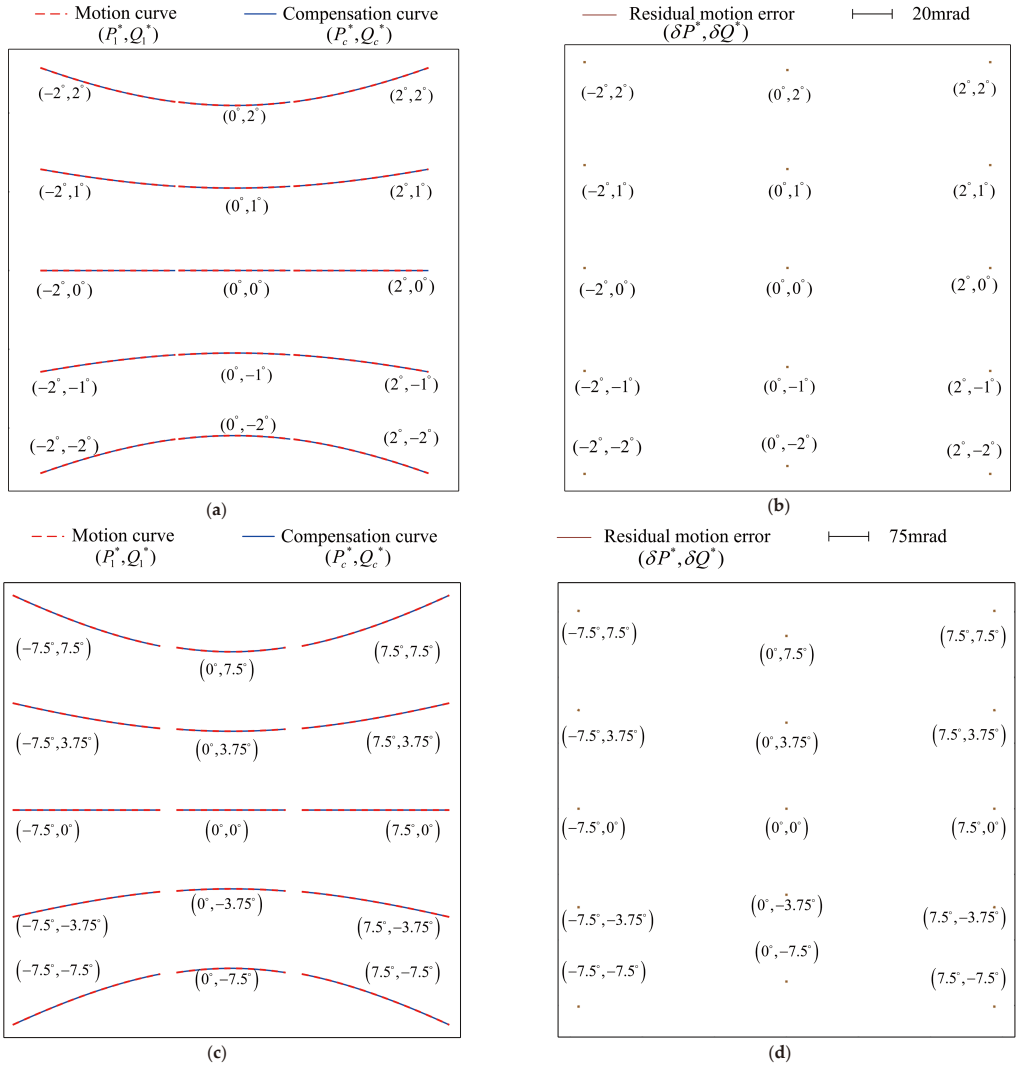


Figure 6. The dynamic motion curves, compensation curves, and residual motion compensation errors under the planar-symmetric fore-afocal lens mapping. (**a**) The dynamic motion curves and compensation curves, m = 8, IFOV = 4° × 4°, w = 400°/s, T = 5 ms. (**b**) The residual motion compensation errors, m = 8, IFOV = 4° × 4°, w = 400°/s, T = 5 ms. (**c**) The dynamic motion curves and compensation curves, m = 4, IFOV = 15° × 15°, w = 720°/s, T = 9 ms. (**d**) The residual motion compensation errors, m = 4, IFOV = 15° × 15°, w = 720°/s, T = 9 ms.

The above analysis also demonstrates that the planar-symmetric mapping given by Equation (14) is general and can accommodate different magnifications, IFOVs, scanning speeds, and exposure times.

3. Optical Design Implementation Method

In this section, we discuss the optical design implementation method of the planar-symmetric fore-afocal lens mapping derived in Section 2.2.

As presented by Equation (14) and Figure 5, the new mapping exhibits different magnifications in the horizontal and vertical directions, displaying planar-symmetric anamorphic characteristics. Therefore, design methods for anamorphic optical systems can be drawn upon in its optical design implementation. A variety of design methods for anamorphic optical systems have been reported in the literature, including combinations of a freeform front group with an aspheric rear group [14], combinations of freeform surfaces with even aspheric surfaces [15], combinations of a conventional aperture lens group with a freeform field lens group [16], cylindrical lens groups [18], and tilted and decentered lens groups [19]. Among these, freeform optics are particularly advantageous due to their abundant design degrees and superior correction capabilities. We thus employ freeform elements for optical design implementation.

Since the planar-symmetric mapping closely resembles the axisymmetric mapping in its low-order characteristics, the initial axisymmetric fore-afocal lens can be adopted as the starting configuration for the design, thereby avoiding a lengthy and complex from-scratch design process. To realize the planar-symmetric mapping characteristics, the method proposed by H.J. Mann et al. is employed by adding a freeform field lens group inside the axisymmetric fore-afocal lens [16], thereby adjusting the axisymmetric mapping into the desired planar-symmetric mapping characteristics, as shown in Figure 7.

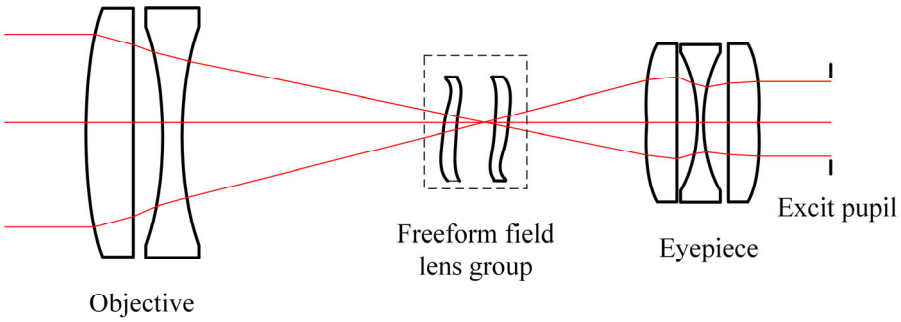


Figure 7. Schematic of the planar-symmetric fore-afocal lens optical design implementation.

Freeform surfaces can be represented by XY polynomials, Zernike polynomials, splines, or other types. In this work, the XY polynomial type is chosen for optical design due to its simple and direct characterization of the surface profile.

To accurately realize the planar-symmetric mapping expressed by Equation (14), the surface profiles, thicknesses, and spacings of the elements must be further optimized. This can be accomplished using commercial optical design software; in this study, Code V 11.2 is used. The merit function Ψ for optimization needs to be redesigned, as shown below:

$$\Psi = \Psi_W + \Psi_C + \Psi_M \tag{17}$$

Here, Ψ_W denotes a composite wavefront error variance function available by default in Code V, used to minimize the wavefront aberrations of the output ray beams and thereby ensure image quality. The expression for Ψ_W is:

$$\Psi_W = \sum_i \sum_\lambda \sum_j \omega_i \omega_\lambda \omega_j {OPD_{i,\lambda,j}}^2 \tag{18}$$

where i denotes the field sampling index, λ denotes the wavelength sampling index, and j denotes the pupil sampling index. $OPD_{i,\lambda,j}$ denotes the optical path difference relative to the reference-wavelength chief ray, and ω_i, ω_λ, and ω_j are the weighting factors for field, wavelength, and pupil position, respectively. Ψ_C is a composite physical structural boundary constraint function that includes the entrance pupil position, exit pupil position, total optical system length, etc.; it can be defined directly using the special constraint commands provided by Code V. $\Psi_{\mathcal{M}}$ is a user-defined constraint representing the max mapping deviation relative to the theoretical value given by Equation (14), expressed as:

$$\Psi_{\mathcal{M}} = \mathrm{Max}\left(\sqrt{\left(\bar{\mathcal{M}}_x(p_i, q_i) - \mathcal{M}_x(p_i, q_i) \right)^2 + \left(\bar{\mathcal{M}}_y(p_i, q_i) - \mathcal{M}_y(p_i, q_i) \right)^2} \right) \tag{19}$$

Here, (p_i,q_i) denotes the directional tangents of the incident reference-wavelength chief ray from the ith sampled field position in object space; $\bar{\mathcal{M}}_x(p_i, q_i)$ and $\bar{\mathcal{M}}_y(p_i, q_i)$ are the actual directional tangents of the output chief ray; $\mathcal{M}_x(p_i,q_i)$ and $\mathcal{M}_y(p_i,q_i)$ are the theoretical values given by Equation (14). As analyzed in Section 2.2, the mapping curve given by Equation (14) coincides with the retrace compensation curve. Thus, the smaller the value of $\Psi_{\mathcal{M}}$, the smaller the residual error after retrace compensation. During optimization, the threshold for $\Psi_{\mathcal{M}}$ can be set based on the maximum residual error acceptable to the system.

In optimization, the wavefront error, structural constraints, and mapping error constraints may compete with one another, leading to convergence difficulties. A balance can be achieved by tuning the weighting factors in Equation (18) and the stiffness of the constraint functions. If such competition prevents convergence or the merit function from meeting its target, the design degrees of freedom can be increased, for example, by adding elements or aspherical surfaces, until the design goal is reached. Additionally, a trade-off between the mapping accuracy and the complexity of the freeform elements is required. A higher order and larger number of freeform surfaces enable more accurate mapping but reduce practical feasibility. Thus, optimization can begin with a few low-order freeform surfaces; if the required mapping accuracy is not achieved, the number and order are progressively increased until the mapping accuracy meets the target.

4. Case Study and Validation

The effectiveness of the proposed theory and method is validated through optical simulations and comparative analyses, conducted with a mid-wave infrared backscanning step-and-stare imaging system as a case study. The exemplary system consists of an 8× fore-afocal lens, a retrace mirror, an imaging lens, and a staring-array detector. The system focal length is 450 mm, with an object-space IFOV of 4° × 4°, under working conditions of scanning speed of 400°/s and exposure time of 5 ms. The first-order parameters and operation conditions of the example system are listed in Table 1.

We first perform a simulation for the case employing an axisymmetric fore-afocal lens (see Figure 8), which is carefully designed such that its angular magnification linearity error is less than 10^{-4}, so as to avoid any influence on the simulation. Within the single-frame exposure time of the scanning process, 21 equally spaced instantaneous time points, including the start and end points, are sampled for ray tracing, calculation, and analysis. Multiple field positions are selected within the IFOV for evaluation. This temporal time

sampling is adequate for the simulation and evaluation, because adding more sampling points no longer improves convergence.

Table 1. First-order parameters and operation conditions of the example system.

Parameter	Value
Wavelength	3.7~4.8 μm
IFOV	4° × 4°
F number	3
System focal length	450 mm
Entrance Pupil Diameter	150 mm
Magnification of the fore-afocal lens	8×
Focal length of the imaging lens	56.25 mm
Scanning angular rate of the gimbal	400°/s
Exposure time	5 ms

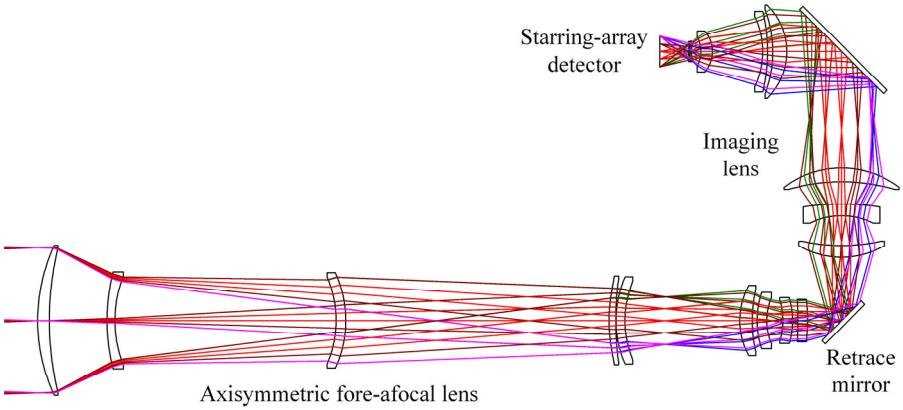


Figure 8. Optical layout of the example system with axisymmetric fore-afocal lens.

The position difference of the reference-wavelength (4.1 μm) chief ray on the focal plane between the beginning and end of the exposure time is used to characterize the max motion blur caused by the residual motion compensation error:

$$\delta L = \sqrt{(X_e - X_0)^2 + (Y_e - Y_0)^2} \tag{20}$$

Here, δL represents the max motion blur, (X_e, Y_e) denotes the reference-wavelength chief ray position on the focal plane at the end point of the exposure, and (X_0, Y_0) denotes that at the start of the exposure.

The transient spot diagrams on the image plane at each temporal time point are superposed to obtain the scanning imaging spot diagram. The dynamic root mean square (RMS) diameter is calculated to evaluate the scanning image performance:

$$D_{RMS} = 2\sqrt{\frac{\sum_k \sum_\lambda \sum_j \left(\left(x_{k,\lambda,j} - \overline{x}_{k,\lambda,j} \right)^2 + \left(y_{k,\lambda,j} - \overline{y}_{k,\lambda,j} \right)^2 \right)}{\sum_k \sum_j \sum_\lambda}} \tag{21}$$

where D_{RMS} represents the dynamic RMS diameter, $(x_{k,\lambda,j}, y_{k,\lambda,j})$ denotes ray position on the focal plane, and $(\overline{x}_{k,\lambda,j}, \overline{y}_{k,\lambda,j})$ is the ray-position centroid. j is the pupil ray sampling index (192 rays per field), λ is the wavelength sampling index (three wavelengths: 3.7 μm, 4.1 μm, and 4.8 μm), and k is the temporal time sampling index during scanning (21 time points in total).

Figure 9a presents the static imaging spot diagrams, along with the static RMS diameters. Figure 9b presents the scanning imaging spot diagrams, in which the red curves indicate the motion trajectories of the chief rays on the image plane during single-frame exposure; the dynamic RMS diameters are also given. The results show that under axisymmetric fore-afocal lens mapping, severe motion blur exists at off-axis fields out of the centerline, consistent with the theoretical analysis in Section 2.1. The residual motion compensation errors transform the spot diagrams into curved streaks, and the dynamic RMS diameters increase significantly compared to the static RMS diameters. At the most severely affected position, the motion blur reaches 607 μm, and the RMS diameter of the spot diagram increases from 35.3 μm in the static case to 376 μm in the dynamic case, which is far larger than the typical mid-wave infrared detector pixel size (15 μm or 25 μm).

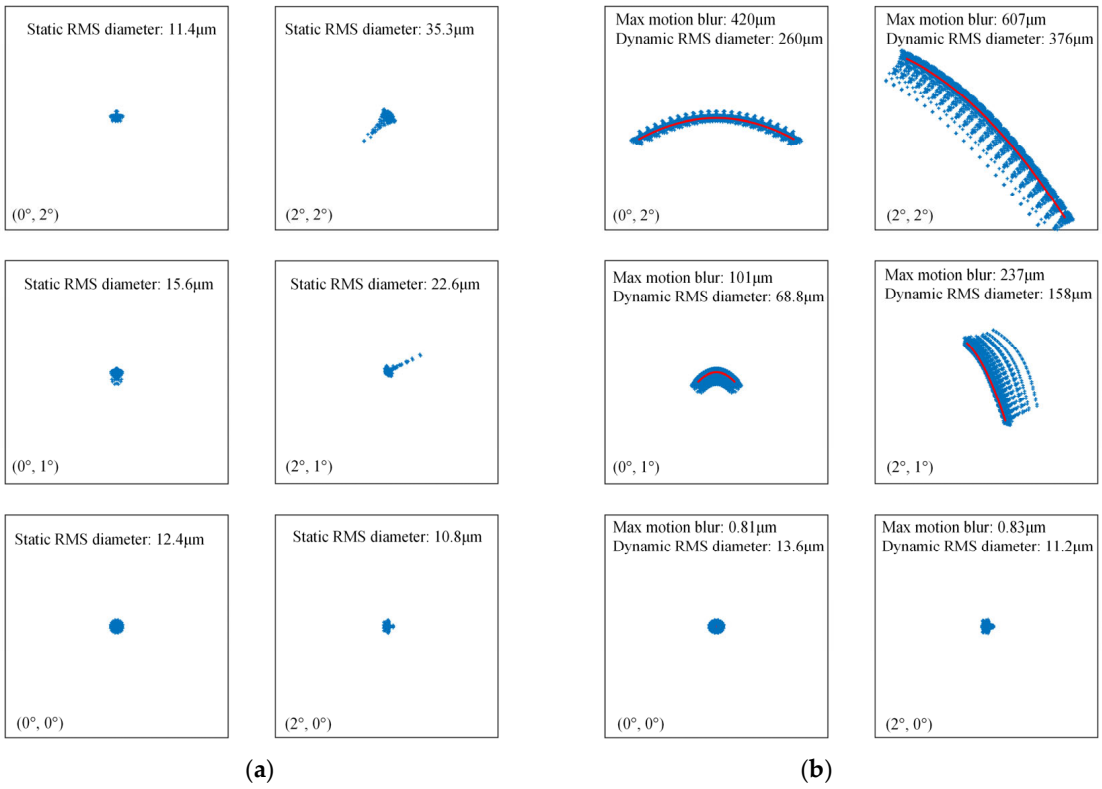


Figure 9. Static and scanning imaging spot diagrams of the exemplary system with the axisymmetric fore-afocal lens. (**a**) The static imaging spot diagrams along with the static RMS diameters. (**b**) The scanning imaging spot diagrams and residual motion trajectories of the chief rays, along with the max motion blur and dynamic RMS diameter.

Subsequently, following the design method presented in Section 3, we take the axisymmetric fore-afocal lens shown in Figure 8 as the starting point to design a new afocal lens that satisfies the planar-symmetric mapping given by Equation (14). Optical optimization is carried out in Code V using three wavelengths (3.7 μm, 4.1 μm, and 4.8 μm). A total of 64 field positions are uniformly sampled in the upper-right quadrant of the IFOV as control points for merit function evaluation and control, while the pupil ray sampling positions and number follow Code V's default settings. After a trade-off between the mapping accuracy and the complexity of the freeform elements, a field lens group with three 10th-order XY-type freeform lenses is utilized, controlling the max mapping error Ψ_M better than 6×10^{-5}. This means that the maximum angular deviation between the actual output ray beams and the theoretical values given by Equation (14) is less than 60 μrad. The final planar-symmetric fore-afocal lens design is shown in Figure 10, with its first-order magnification,

entrance aperture, entrance pupil position, exit pupil position, overall length, and other technical parameters identical to those of the axisymmetric case.

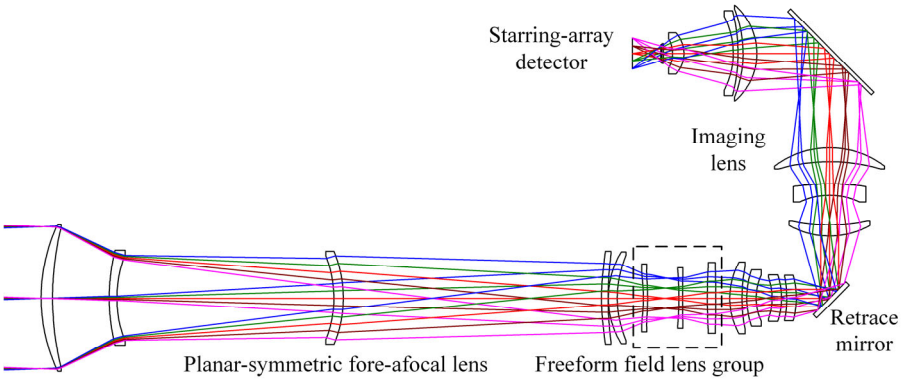


Figure 10. Optical layout of the example system with a planar-symmetric fore-afocal lens.

Lastly, we replace the axisymmetric afocal lens in Figure 8 with the planar-symmetric afocal lens, yielding a new backscanning step-and-stare optical system, as shown in Figure 10. Using the same simulation method for the axisymmetric case, we obtain the static imaging spot diagrams, static RMS diameters, scanning imaging spot diagrams, dynamic RMS diameters, and motion blur, as shown in Figure 11. The results demonstrate that the motion blur caused by the residual motion compensation errors is no more than 3.1 μm, and the dynamic RMS diameter increases by no more than 3.2 μm relative to the static case.

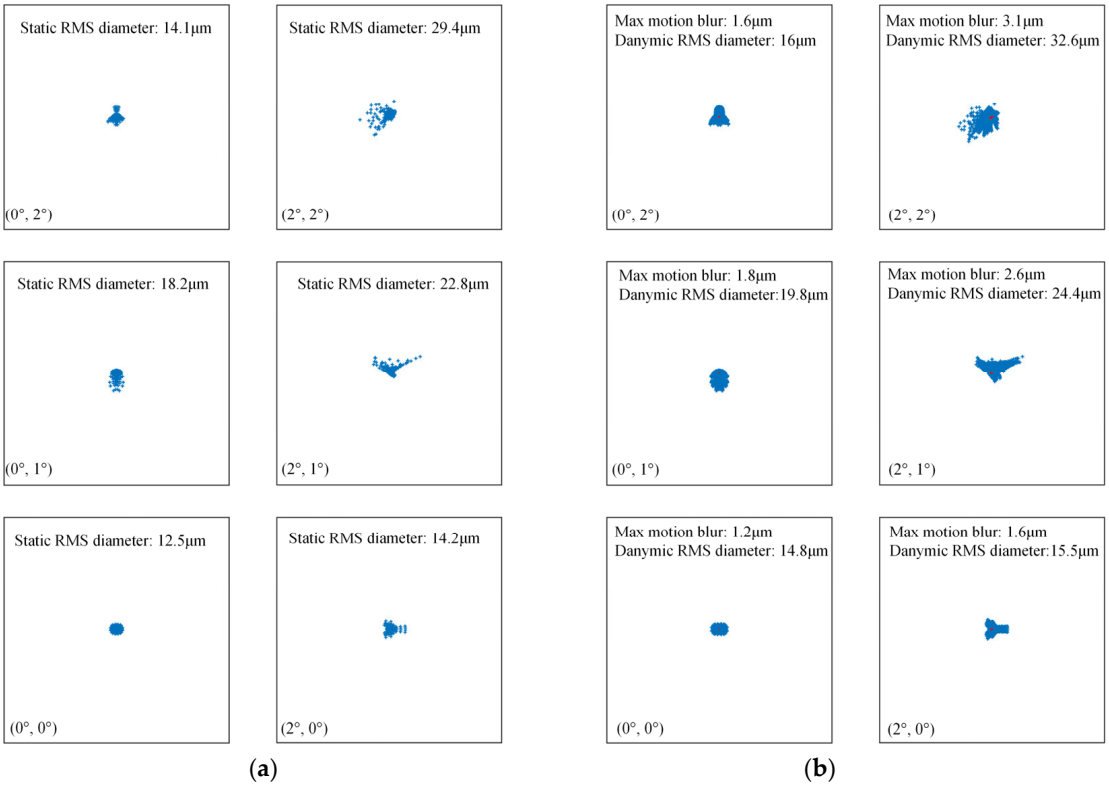


Figure 11. Static and scanning imaging spot diagrams of the exemplary system with the planar-symmetric fore-afocal lens. (**a**) The static imaging spot diagrams along with the static RMS diameters. (**b**) The scanning imaging spot diagrams and residual motion trajectories of the chief rays, along with the max motion blur and dynamic RMS diameter.

As shown in Figure 11, small residual motion blur persists under the planar-symmetric afocal lens mapping. This arises because the optical optimization cannot reduce the merit function to exactly zero, leaving a slight discrepancy between the actual mapping and the theoretical value from Equation (14). Since this residual blur is much smaller than the typical mid-wave infrared detector pixel size, it can be considered effectively suppressed.

5. Discussion

This paper aims to solve the residual motion compensation error problem in backscanning step-and-stare imaging induced by the axisymmetric fore-afocal lens. This error arises because the axisymmetric nature of the fore-afocal lens mapping prevents the off-axis field output rays from rotating uniformly about the rotation axis at the magnified angular rate, so that they cannot be fully compensated. The motion blur induced by this error increases approximately linearly with the scanning speed and integration time, and quadratically with the field position. To overcome this limitation at its source, we derive a planar-symmetric fore-afocal lens mapping that ensures uniform rotational behavior of the output rays during scanning and present a freeform-based optical design implementation method. Validation is carried out through an example design, simulations, and comparative analyses. The results show that the residual motion compensation errors are effectively suppressed after being replaced by the planar-symmetric afocal lens in a simulation environment, since the maximum motion blur caused by the error is reduced from 607 μm to 3.1 μm.

From a theoretical standpoint, compared with existing studies on motion compensation [8–11], this work extends compensation from the line of sight alone to positions across the full IFOV and supports the design and development of systems with a larger IFOV, higher scanning speed, and longer exposure time. In terms of optical design implementation, this paper draws upon an anamorphic lens design method based on freeform optics following the method of H.J. Mann et al. [16]. Starting from the axisymmetric fore-afocal lens, a freeform field lens group is added, and the lens is further optimized to accurately realize the planar-symmetric mapping. This method enables improvement and implementation on the basis of existing axisymmetric systems, avoiding the complex from-scratch design process. In contrast to typical anamorphic lens designs [14,15,18,19], this work broadens the application scope from static anamorphic imaging to the real-time correction of dynamic errors in scanning imaging.

In practice, the residual motion compensation error and motion blur of a conventional axisymmetric system can be estimated using Equations (8) and (9). When the maximum motion blur exceeds an acceptable threshold, the method proposed in this paper can be adopted to improve the system. Although the validation is based on a specific example system, the results are not limited to that case and remain general. Since the proposed planar-symmetric fore-afocal lens mapping theory is general, it is applicable to systems with other parameters (such as different scanning speeds, IFOVs, afocal magnifications, and operating spectral bands), as long as the systems conform to the backscanning step-and-stare imaging architecture and operating principle illustrated in Figure 1.

This study is currently limited to theoretical derivation, method development, and simulation validation. It does not yet account for the influence of manufacturing- and operation-related effects on the compensation and imaging performance, such as element fabrication precision, optical assembly errors, retrace accuracy of the mirror, and thermal effects. These issues are suitable subjects for future work. The next phase of this research will focus on the physical realization and experimental verification of a planar-symmetric afocal lens prototype, including manufacturability-oriented re-optimization, prototype fabrication, and experimental comparison and validation.

6. Conclusions

This paper addresses the residual motion compensation error problem inherent in conventional backscanning step-and-stare imaging with axisymmetric fore-afocal lenses. To solve this issue at its source, we derive a planar symmetric mapping for the fore-afocal lens and present a freeform-based optical design implementation. The proposed mapping theoretically enables residual motion compensation error suppression at different positions across the full IFOV. A mid-wave infrared system is designed and evaluated through comprehensive optical simulations and comparative analyses. After replacing the axisymmetric fore-afocal lens with the planar-symmetric fore-afocal lens, the residual motion compensation errors are effectively suppressed in a simulation environment. The theory and method are general and can provide theoretical and methodological support for backscanning step-and-stare imaging with a larger IFOV, higher scanning speed, and longer exposure time. Future work will focus on manufacturing- and operation-related effect analysis, physical realization, and experimental verification.

Supplementary Materials: The following supporting information can be downloaded at https://www.mdpi.com/article/10.3390/photonics13111034/s1, Table S1: Detailed parameters of example system with axisymmetric fore-afocal lens shown in Figure 7; Table S2: Detailed parameters of the planar-symmetric fore-afocal lens shown in Figure 9.

Author Contributions: Y.L.: Methodology. Y.C.: Writing—original draft. L.W. and X.L.: Case optic system design and simulation. X.C. and Z.H.: Writing—review and editing, conceptualization. J.J.: Validation. All authors have read and agreed to the published version of the manuscript.

Funding: This research received no external funding.

Data Availability Statement: The data presented in this study are available in the article or in the Supplementary Materials.

Conflicts of Interest: The authors declare no conflicts of interest.

Appendix A. Derivation of the Planar-Symmetric Fore-Afcoal Lens Mapping Using the Method of Separation of Variables

Let $\mathcal{M}_x(p_0,q_0) = \mathcal{M}_{xp}(p_0)\mathcal{M}_{xq}(q_0)$ and $\mathcal{M}_y(p_0,q_0) = \mathcal{M}_{yp}(p_0)\mathcal{M}_{yq}(q_0)$, from Equation (13); we have:

$$\mathcal{M}_{xp}\left(\frac{p_0+\tan wt}{1-p_0\tan wt}\right)\mathcal{M}_{xq}\left(\frac{q_0}{\cos wt-p_0\sin wt}\right)=\frac{\mathcal{M}_{xp}(p_0)\mathcal{M}_{xq}(q_0)+\tan(mwt)}{1-\mathcal{M}_{xp}(p_0)\mathcal{M}_{xq}(q_0)\tan(mwt)} \tag{A1}$$

$$\mathcal{M}_{yp}\left(\frac{p_0+\tan wt}{1-p_0\tan wt}\right)\mathcal{M}_{yq}\left(\frac{q_0}{\cos wt-p_0\sin wt}\right)=\frac{\mathcal{M}_{yp}(p_0)\mathcal{M}_{yq}(q_0)}{\cos(mwt)-\mathcal{M}_{xp}(p_0)\mathcal{M}_{xq}(q_0)\sin(mwt)} \tag{A2}$$

When p_0 and q_0 are set to 0, the above expressions still hold and can be written as:

$$\mathcal{M}_{xp}(\tan wt)\mathcal{M}_{xq}(0)=\frac{\mathcal{M}_{xp}(0)\mathcal{M}_{xq}(0)+\tan(mwt)}{1-\mathcal{M}_{xp}(0)\mathcal{M}_{xq}(0)\tan(mwt)} \tag{A3}$$

$$\mathcal{M}_{yp}(\tan wt)\mathcal{M}_{yq}(0)=\frac{\mathcal{M}_{yp}(0)\mathcal{M}_{yq}(0)}{\cos(mwt)-\mathcal{M}_{xp}(0)\mathcal{M}_{xq}(0)\sin(mwt)} \tag{A4}$$

As the "parabasal" property of rays, it follows that $\mathcal{M}_{xp}(0)\mathcal{M}_{xq}(0) = \mathcal{M}_x(0,0) = 0$ and $\mathcal{M}_{yp}(0)\mathcal{M}_{yq}(0) = \mathcal{M}_y(0,0) = 0$. Substituting into Equations (A3) and (A4) and solving yields:

$$\mathcal{M}_{xp}(\tan wt)=\frac{\tan(mwt)}{\mathcal{M}_{xq}(0)} \tag{A5}$$

$$\mathcal{M}_{yq}(0) = 0 \tag{A6}$$

Setting t to zero and substituting into Equation (A5) yields:

$$\mathcal{M}_{xp}(0) = 0 \tag{A7}$$

Substituting p_0 for tanwt in Equation (A5) yields:

$$\mathcal{M}_{xp}(p_0) = \frac{\tan(m\ \tan^{-1} p_0)}{\mathcal{M}_{xq}(0)} \tag{A8}$$

When only p_0 is set to 0, Equations (A1) and (A2) are rewritten as:

$$\mathcal{M}_{xp}(\tan\ wt)\mathcal{M}_{xq}\left(\frac{q_0}{\cos wt}\right) = \frac{\mathcal{M}_{xp}(0)\mathcal{M}_{xq}(q_0) + \tan(mwt)}{1 - \mathcal{M}_{xp}(0)\mathcal{M}_{xq}(q_0)\tan(mwt)} \tag{A9}$$

$$\mathcal{M}_{yp}(\tan\ wt)\mathcal{M}_{yq}\left(\frac{q_0}{\cos wt}\right) = \frac{\mathcal{M}_{yp}(0)\mathcal{M}_{yq}(q_0)}{\cos(mwt) - \mathcal{M}_{xp}(0)\mathcal{M}_{xq}(q_0)\sin(mwt)} \tag{A10}$$

Substituting Equations (A5) and (A7) into Equation (A9), solving yields:

$$\mathcal{M}_{xq}\left(\frac{q_0}{\cos w}\right) = \mathcal{M}_{xq}(0) \tag{A11}$$

The above expression indicates that the operator $\mathcal{M}_{xq}$ maps all variables to a constant, and therefore:

$$\mathcal{M}_{xq}(q_0) = \mathcal{M}_{xq}(0) \tag{A12}$$

Substituting Equation (A7) into Equation (A10), solving yields:

$$\frac{\mathcal{M}_{yp}(\tan wt)\cos(mwt)}{\mathcal{M}_{yp}(0)} = \frac{\mathcal{M}_{yq}(q_0)}{\mathcal{M}_{yq}\left(\frac{q_0}{\cos wt}\right)} \tag{A13}$$

The above expression holds for any w and t; therefore, $\mathcal{M}_{yq}(q_0)$ must be linear in q_0:

$$\mathcal{M}_{yq}(q_0) \propto q_0 \tag{A14}$$

From the above expression, we have $\mathcal{M}_{yq}(q_0) = \cos(wt)\mathcal{M}_{yq}\left(\frac{q_0}{\cos(wt)}\right)$. Substituting this into Equation (A13) yields:

$$\mathcal{M}_{yp}(\tan(wt)) = \frac{\cos(wt)}{\cos(mwt)}\mathcal{M}_{yp}(0) \tag{A15}$$

Substituting p_0 for tanwt in Equation (A15) yields:

$$\mathcal{M}_{yp}(p_0) = \frac{\cos(\tan^{-1} p_0)}{\cos(m\ \tan^{-1} p_0)}\mathcal{M}_{yp}(0) \tag{A16}$$

Using Equations (A8), (A12), (A14) and (A16), we obtain:

$$\mathcal{M}_x(p_0,q_0) = \mathcal{M}_{xp}(p_0)\mathcal{M}_{xq}(q_0) = \tan(m\ \tan^{-1}p_0) \tag{A17}$$

$$\mathcal{M}_y(p_0,q_0) = \mathcal{M}_{yp}(p_0)\mathcal{M}_{yq}(q_0) = \gamma\mathcal{M}_{yp}(0)\frac{\cos(\tan^{-1} p_0)}{\cos(m\ \tan^{-1} p_0)}q_0 \tag{A18}$$

where γ is a quantity that does not depend on q_0. Performing a series expansion on Equation (A18), the coefficient of the first-order term in q_0 is found to be $\gamma\mathcal{M}_{yp}(0)$. Since the mapping function $\mathcal{M}_y(p_0,q_0)$ is required to satisfy the prerequisite that the first-order angular magnification is m, we have $\gamma\mathcal{M}_{yp}(0) = m$. Substituting into Equation (A18), the analytical expressions of the $\mathcal{M}_x(p_0,q_0)$ and $\mathcal{M}_y(p_0,q_0)$ are finally obtained as:

$$\mathcal{M}_x(p_0,q_0) = \tan(m\ \tan^{-1}p_0) \tag{A19}$$

$$\mathcal{M}_y(p_0,q_0) = m\frac{\cos(\tan^{-1} p_0)}{\cos(m\ \tan^{-1} p_0)}q_0 \tag{A20}$$

References

1. John Lester, M.; Scott, W.; Bruce, E.; Cynthia, A. Design challenges regarding high-definition electro-optic/infrared stabilized imaging systems. *Opt. Eng.* **2013**, *52*, 061310. [CrossRef]
2. Sun, C.; Ding, Y.; Wang, D.; Tian, D. Backscanning step and stare imaging system with high frame rate and wide coverage. *Appl. Opt.* **2015**, *54*, 4960–4965. [CrossRef]
3. Ronald, D.; Eytan, P.; Robert, G.; Ectis, V.; Robert, S.; Gerald, H.; Orges, F. Detection of small targets in the infrared: An infrared search and track tutorial. *Appl. Opt.* **2021**, *60*, 4762–4777. [CrossRef]
4. Luu, T.V. Design a short-time backscanning profile for IRST application. In *Proceedings of the Electro-Optical and Infrared Systems: Technology and Applications XVIII and Electro-Optical Remote Sensing XV 2021, Online, Spain, 13–17 September 2021*; SPIE: Bellingham, WA, USA, 2021; p. 118660N.
5. Dat, N.V.; Du, D.X.; Dat, V.X. Optical design for multi-functional IRST system using high-definition detector. In *Proceedings of the Optical Design and Testing XII, Online, China, 21 December 2022*; SPIE: Bellingham, WA, USA, 2022; p. 123150Y.
6. Pierre-Olivier, N.; Paul, B.; Flavien, R.; Jean-François, O.; Mathieu, R. Third-generation naval IRST using the step-and-stare architecture. In *Proceedings of the 34th Conference on Infrared Technology and Applications, Orlando, FL, USA, 17–20 March 2008*; SPIE: Bellingham, WA, USA, 2008; Volume 4940, p. 69401B.
7. Dominique, M.; Olivier, D.; Guillaume, V.; Carole, P.; Gisèle, H.; Pierre-Olivier, N. New generation of Naval IRST: Example of EOMS NG. In *Proceedings of the Infrared Technology and Applications XXXVI, Orlando, FL, USA, 5–9 April 2010*; SPIE: Bellingham, WA, USA, 2010; Volume 7660, p. 766004.
8. Sun, J.; Ding, Y.; Zhang, H.; Yuan, G.; Zheng, Y. Conceptual design and image motion compensation rate analysis of two-axis fast steering mirror for dynamic scan and stare imaging system. *Sensors* **2021**, *21*, 6441–6463. [CrossRef]
9. Gao, P.; Su, X.; Pan, Z.; Liu, R.; Zhang, W.; Cao, Y.; Wang, L. Image motion compensation control method for the dynamic scan and stare imaging system. *Appl. Opt.* **2021**, *63*, 8890–8897.
10. Wang, L.; Liu, X.; Wang, C. Modeling and design of fast steering mirror in image motion compensation for backscanning step and stare imaging systems. *Opt. Eng.* **2019**, *58*, 103105. [CrossRef]
11. Tian, D.; Wang, Y.; Wang, Z.; Wang, F.; Gao, H. Long integral time continuous panorama scanning imaging based on bilateral control with image motion compensation. *Remote Sens.* **2019**, *11*, 1924. [CrossRef]
12. Li, Y.; Cui, T.; Li, Q.; Zhang, B.; Bai, Y.; Wang, C. A study of correction method to the pincushion distortion based on dual galvanometer LiDAR scanning system. *Optik* **2019**, *181*, 555–561. [CrossRef]
13. Dehoog, E.A. Anamorphic zoom lens based on rotating cylindrical lenses. *Opt. Express* **2021**, *29*, 422097. [CrossRef]
14. Xu, C.; Song, W.; Wang, Y. Design of a miniature anamorphic lens with a freeform front group and an aspheric rear group. *Opt. Eng.* **2021**, *60*, 065104. [CrossRef]
15. Zhuang, Z.; Parent, J.; Roulet, P.; Thibault, S. Freeform wide-angle camera lens enabling mitigable distortion. *Appl. Opt.* **2022**, *61*, 185449. [CrossRef]
16. Mann, H.J.; Ulrich, W. Reflective high-NA projection lenses. In *Proceedings of the SPIE, Optical Design and Engineering II, Jena, Germany, 12–16 September 2005*; SPIE: Bellingham, WA, USA, 2005; p. 596214.
17. Liu, Y.; Jin, W.Q.; Zhu, B. Analytical expressions of the imaging and aberration coefficients of a general form surface. *J. Opt. Soc. Am. A* **2017**, *34*, 2077–2095. [CrossRef]
18. Zhang, J.; Wang, X.; Chen, X.; Liu, H.; Li, F.; Sun, X. Paraxial lens design of anamorphic lenses with double telecentricity. *OSA Contin.* **2019**, *2*, 366719. [CrossRef]
19. Zhang, X.; Wang, L.; Yu, J.; Jin, C. Design of tilted and decentered anamorphic optical system based on nodal aberration control. *Optik* **2023**, *290*, 171128. [CrossRef]

Disclaimer/Publisher's Note: The statements, opinions and data contained in all publications are solely those of the individual author(s) and contributor(s) and not of MDPI and/or the editor(s). MDPI and/or the editor(s) disclaim responsibility for any injury to people or property resulting from any ideas, methods, instructions or products referred to in the content.